Integrated-Photonics Devices and Architectures for Advanced Cooling of Trapped Ions

by

Ashton Hattori

B.S., Georgia Institute of Technology (2020)

Submitted to the
Department of Electrical Engineering and Computer Science
in partial fulfillment of the requirements for the degree of

Master of Science

at the

MASSACHUSETTS INSTITUTE OF TECHNOLOGY

September 2023

© Ashton Hattori 2023. All rights reserved.

The author hereby grants to MIT a nonexclusive, worldwide, irrevocable, royalty-free license to exercise any and all rights under copyright, including to reproduce, preserve, distribute and publicly display copies of the thesis, or release the thesis under an open-access license.

Authored by: Ashton Hattori
Department of Electrical Engineering and Computer Science
August 31, 2023

Certified by: Jelena Notaros
Robert J. Shillman (1974) Career Development Assistant Professor of Electrical and Computer Engineering
Thesis Supervisor

Accepted by: Leslie A. Kolodziejski
Professor of Electrical Engineering and Computer Science
Chair, Department Committee on Graduate Students

Integrated-Photonics Devices and Architectures for Advanced Cooling of Trapped Ions

by

Ashton Hattori

Submitted to the Department of Electrical Engineering and Computer Science
on August 31, 2023, in partial fulfillment of the
requirements for the degree of
Master of Science

Abstract

Integrated-photonics-based architectures for trapped-ion systems offer a potential avenue for improved fidelity and addressability of ion arrays. Motional state cooling, a key optical function in trapped-ion systems, however, has been limited to Doppler and resolved-sideband cooling in integrated-photonics-based implementations. In contrast, polarization-gradient and electromagnetically-induced-transparency cooling can offer better cooling performance in multi-ion systems, but have not been demonstrated on an integrated-photonics platform. This thesis demonstrates key integrated-photonics devices and architectures to enable enhanced laser cooling of integrated trapped-ion systems.

First, we develop the framework for two advanced trapped-ion cooling schemes, polarization-gradient and electromagnetically-induced-transparency cooling. Then, we present the design of key integrated devices enabling the proposed system architectures. First, we show the design and experimental demonstration of the first integrated polarization splitters and rotators at blue wavelengths. We develop compact and efficient designs for both a polarization splitter and rotator at a 422-nm wavelength, an important transition for $^{88}Sr^{+}$ ions. These devices are fabricated in a 200-mm wafer-scale process and experimental results are demonstrated. Next, we present the design and experimental demonstration of the first pair of integrated TE- and TM-emitting gratings at a wavelength of 422 nm to enable polarization-diverse operations for integrated-photonics-based trapped-ion systems. The development of both the devices and architectures for advanced cooling schemes presented in this thesis paves the way for sophisticated integrated control for trapped-ion and neutral-atom systems.

Thesis Supervisor: Jelena Notaros

Title: Robert J. Shillman (1974) Career Development Assistant Professor of Electrical Engineering and Computer Science

Acknowledgments

Firstly, I would like to thank my advisor and PI, Professor Jelena Notaros, for her guidance and support. I am especially thankful for her ability to teach any concept, no matter how complicated, in a way that is understandable and accessible; I have truly learned so much from her.

This work would not have been possible without the support of my fellow group-mates in the Photonics and Electronics Research Group. I would like to give a special thank you to Milica Notaros, whose insight and mentorship has been invaluable to me over the past two years. Additionally, I would like to thank Sabrina Corsetti, Tal Sneh, Andres Garcia Coleto, Daniel DeSantis, and Michael Torres for both their helpful insights and for their friendship. They have been a source of joy and laughter in my life, and I am so thankful to them.

Next, I would like to thank my collaborators at MIT Lincoln Laboratory and MIT: Dr. Reuel Swint, Dr. Patrick T. Callahan, Dr. Cheryl Sorace-Agaskar, Dr. Dave Kharas, Dr. Thomas Mahony, Dr. Colin D. Bruzewicz, Gavin N. West, Felix Knollman, Dr. Ethan R. Clements, Dr. Robert McConnell, and Dr. John Chiaverini for their useful discussions and input. I would particularly like to thank Robert and John, whose invaluable support has allowed us to pursue this project, and whose wit and insight has made every Tuesday morning meeting exciting.

Additionally, I would like to thank my mentors, both at Georgia Tech and at MIT. At Georgia Tech, I would like to thank my undergraduate advisors, Dr. Benjamin Yang and Professor Thomas K. Gaylord, without whom, I would not be where I am today. I would also like to thank Dr. Paloma Casteleiro-Costa, who has given endless mentorship, support, and, most importantly, friendship over the past six years. At MIT, I would like to thank Professor Leslie Kolodziejski, who has been a wonderful source of invaluable advice and support.

I would also like to thank the EECS and RLE staff, without whom, nothing would get done. In particular, I would like to thank Dianne Lior, Janet Fischer, Alicia Duarte, Liza Ruano, William Gibbs, and William Adams for their administrative

and technical support.

Finally, I would like to thank my friends and family. In particular, I would like to thank my brother, Austin, who has always been a source of inspiration, and for my sister April, for being the reason I strive to be a better person. I would like to thank my friends Kathryn, Lane, Jasmine, Nia, Grace, and Sabrina, whose love and friendship have been invaluable to me. Finally, I would like to thank my partner, Stephanie. She has made my life better in every way, and words cannot begin to express how thankful I am for her love and support.

Funding: This work was supported by National Science Foundation (NSF) QLCI HQAN (2016136), NSF QLCI Q-SEnSE (2016244), MIT Center for Quantum Engineering (H98230-19-C-0292), and the National Defense Science and Engineering Graduate (NDSEG) Fellowship Program.

Contents

List of Figures

Chapter 1

Introduction

1.1 Introduction to Integrated Photonics for Trapped-Ion Systems

Systems of trapped ions are a promising modality for quantum information processing due to their long coherence times and strong ion-ion interactions, which enable high-fidelity two-qubit gates [1]. Most current implementations, however, are comprised of complex free-space optical systems whose large size and susceptibility to vibrations and drift can limit fidelity and addressability of ion arrays, hindering scaling to large numbers of qubits. Recent works based on integrated photonic devices offer a potential avenue to address many of these challenges [1–9].

Typical integrated realization of trapped-ion systems consists of using integrated surface electrodes to form a linear-ion-trap geometry, where a radiofrequency oscillating electric field is applied to trap the ion radially in two dimensions, while a DC electric field traps the ions axially in the third dimension [1]. Underneath the trap electrodes, photonic devices route and control the optical fields necessary for trapped-ion state preparation, control, and readout. Wavelengths of interest span from ultraviolet (UV) to infrared (IR), which necessitates low-loss platforms for a wide range of wavelengths [10]. To interface with the ion, photonic gratings emit light vertically towards the ion. An example integrated-photonics trapped-ion system is demonstrated in [2]

(Fig. 1.1), consisting of light of different wavelengths coupled on chip using a fiber array, routed using a single-mode waveguides, and emitting vertically to interface with the ion using focusing gratings.

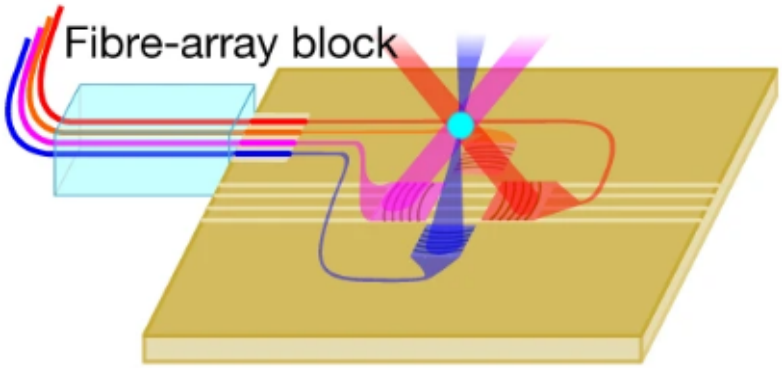

Figure 1.1: An example integrated-photonic trapped-ion system, consisting of light of four different wavelengths coupled on-chip using a fiber array, routed using single-mode waveguides, and emitting vertically using focusing grating couplers. Figure taken from [2].

While integrated-photonic control of trapped ions have been demonstrated, motional state cooling, a key optical function in trapped-ion systems, has been limited to Doppler and resolved-sideband cooling in integrated-photonics-based solutions [2, 3]. However, polarization-gradient (PG) and electromagnetically-induced-transparency (EIT) cooling can offer better cooling performance in multi-ion systems, where sub-Doppler temperatures in several non-degenerate modes are desirable. While free-space demonstrations of these cooling schemes have been shown [11, 12], each having an advantage for differing applications, integrated versions of these systems have not yet been realized.

1.2 Thesis Overview

This thesis demonstrates key integrated-photonics devices and architectures to enable enhanced laser cooling of integrated trapped-ion systems.

In Chapter 2, we propose integrated-photonics-based system architectures and the design of key integrated photonic components for both PG and EIT cooling of trapped

ions. Specifically, we design the systems for a wavelength of 422 nm to target the $S_{1/2}$ to $P_{1/2}$ transition of $^{88}Sr^{+}$, a commonly used ion species for trapped-ion qubits.

Next, in Chapter 3, we present the design and experimental demonstration of the first integrated polarization splitters and rotators at blue wavelengths, which enable the polarization diversity required by the proposed PG and EIT cooling systems. We design and fabricate for the challenging wavelength of 422 nm. To realize visible-wavelength polarization diversity, the polarization splitter uses an asymmetric-directional-coupler design to split the polarizations efficiently and compactly. The polarization rotator uses a mode-coupling design, which has the advantage of being able to rotate the polarization in a compact length. Next, these devices are fabricated using the MIT Lincoln Laboratory 200-mm wafer-scale process for trapped-ion applications, consisting of one layer of alumina and two layers of silicon nitride with a silicon-dioxide cladding. Finally, the performance of the devices is experimentally demonstrated, resulting in a measured polarization-splitter transverse-electric (TE) thru-port coupling of 98.0% and transverse-magnetic (TM) tap-port coupling of 77.6% for a compact length of 16 µm and a polarization-rotator conversion efficiency of 92.2% for a compact length of 111 µm. This work paves the way for more sophisticated integrated control of trapped-ion and neutral-atom quantum systems.

Finally, in Chapter 4, we present the design and experimental demonstration of a pair of integrated TE- and TM-emitting gratings with an operating wavelength of 422 nm, another vital set of devices for realizing PG and EIT cooling schemes. We implement a custom optimization-based design algorithm to realize bilayer, apodized, and curved gratings that emit unidirectional focused beams, with experimentally measured spot dimensions of 7.6 µm by 4.3 µm for the TE grating and 5.0 µm by 3.6 µm for the TM grating at a target ion height of 50 µm above the surface of the chip. This work represents, to the best of our knowledge, the first development of integrated TM-emitting gratings for trapped-ion systems, and, thus, a fundamental stepping stone on the path to advanced operations for integrated-photonics-based trapped-ion quantum systems involving multiple polarizations.

Chapter 2

Integrated-Photonics-Based Architectures for Advanced Cooling of Trapped Ions

The following work was done in collaboration Sabrina Corsetti (MIT), Tal Sneh (MIT), Milica Notaros (MIT), Reuel Swint (MIT Lincoln Laboratory), Patrick T. Callahan (MIT Lincoln Laboratory), Colin D. Bruzewicz (MIT Lincoln Laboratory), Felix Knollmann (MIT), Robert McConnell (MIT Lincoln Laboratory), John Chiaverini (MIT Lincoln Laboratory), and Jelena Notaros (MIT). This work has been published in [13].

2.1 Introduction

As discussed in Chapter 1, systems of trapped ions are a promising modality for quantum information processing due to their long coherence times and strong ion-ion interactions, which enable high-fidelity two-qubit gates [1]. Most current implementations are comprised of complex free-space optical systems, whose large size and susceptibility to vibrations and drift can limit fidelity and addressability of ion arrays, hindering scaling to large numbers of qubits. Recent works based on integrated photonic devices offer a potential avenue to address many of these challenges [1–9].

Motional state cooling is a key optical function in trapped-ion systems. To date, integrated-photonics-based cooling demonstrations have been limited to Doppler and resolved-sideband cooling [2, 3]. However, polarization-gradient (PG) and electromagnetically-induced-transparency (EIT) cooling can offer better cooling performance in multi-ion systems, where sub-Doppler temperatures in several non-degenerate modes are desirable. While free-space demonstrations of these cooling schemes have been shown [11,12], each having an advantage for differing applications, integrated versions of these systems have not yet been realized.

In this chapter, we propose integrated-photonics-based system architectures and the design of key integrated photonic components for both PG and EIT cooling of trapped ions (conceptual diagram shown in Fig. 2.1). Specifically, we design the systems for a wavelength of 422 nm to target the $S_{1/2}$ to $P_{1/2}$ transition of $^{88}Sr^{+}$, a commonly used ion species for trapped-ion qubits.

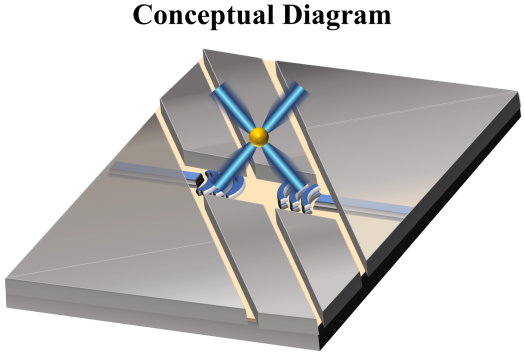

Figure 2.1: Conceptual diagram of the integrated PG-cooling system.

2.2 Integrated-Photonics-Based System Architectures for Trapped-Ion Cooling

We leverage a 200-mm wafer-scale visible-wavelength process developed at MIT Lincoln Laboratory to enable low-loss waveguide fabrication over a wavelength range relevant to commonly used ion species [10]. The platform consists of two bottom layers of 100-nm-thick silicon nitride (Si_3N_4) and an upper layer of 100-nm-thick alumina

(Al_2O_3) separated by 90 nm of silicon dioxide (SiO_2). A top metal layer is etched to create linear-ion-trap electrodes that confine ions 50 μm above the trap surface via radio-frequency and DC voltages [1].

2.2.1 Polarization-Gradient-Cooling System Architecture

Trapped ions located in a suitable laser-polarization gradient can achieve sub-Doppler temperatures due to the preferential scattering of cooling photons in a spatially-varying, state-dependent energy potential [11]. Appropriate polarization gradients can be realized on-chip using different configurations of integrated grating couplers; for example, two transverse-electric (TE) gratings placed orthogonal to each other (TE-TE), a TE and transverse-magnetic (TM) grating placed opposite to each other (TE-TM), or two TM gratings placed opposite to each other (TM-TM) all suffice. The simulated emission profiles for gratings specifically designed for TE and TM are shown in Fig. 2.3 (introduced in detail in Chapter 4). Both gratings are designed to match intensity and focus near the ion at an angle of 45°, maximizing intensity at the ion location. More information on the design and experimental results of TE and TM gratings for PG and EIT cooling can be found in Chapter 4. In all three polarization configurations, light is routed to these gratings via two separate inverse-taper edge couplers and a combination of 650-nm-wide alumina waveguides, 300-nm-wide dual-layer silicon-nitride waveguides, and vertical transitions between layers. The final proposed architectures for PG cooling are shown in Fig. 2.2a–b.

2.2.2 EIT-Cooling System Architecture

EIT cooling enables near ground-state cooling over a wide frequency range by suppressing unwanted heating mechanisms otherwise incurred during laser cooling. Previous free-space demonstrations have relied on two appropriately-polarized laser sources (one circular and one linear) to create the desired laser absorption profile [12].

Fig. 2.4 depicts integrated realization of both the circular and linear sources. To generate the circularly polarized source, light is coupled on chip via an inverse-taper

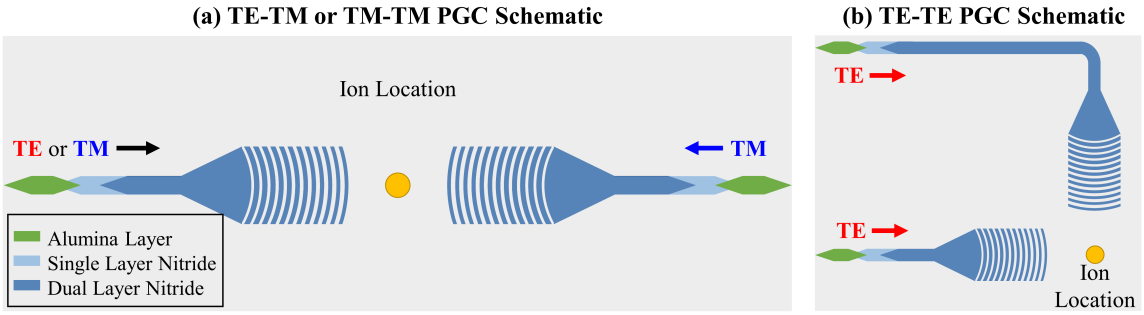

Figure 2.2: Simplified schematics showing the proposed integrated-photonics-based architectures for (a) TE-TM or TM-TM PG cooling and (b) TE-TE PG cooling (not to scale).

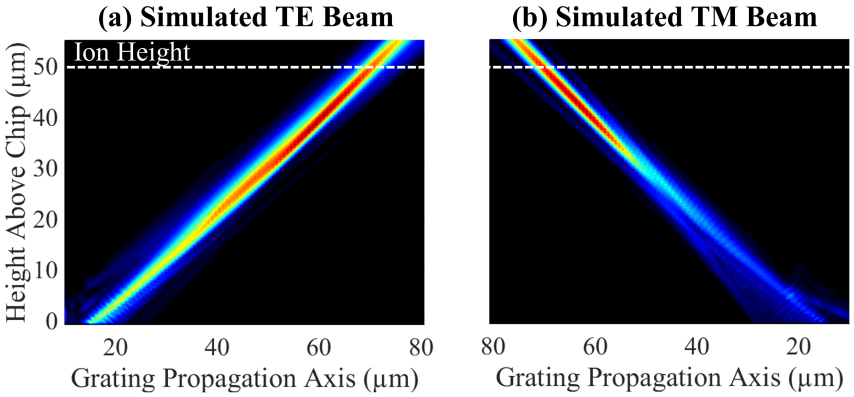

Figure 2.3: Simulated emission profiles for the (a) TE grating and (b) TM grating, showing focusing near the height of the ion.

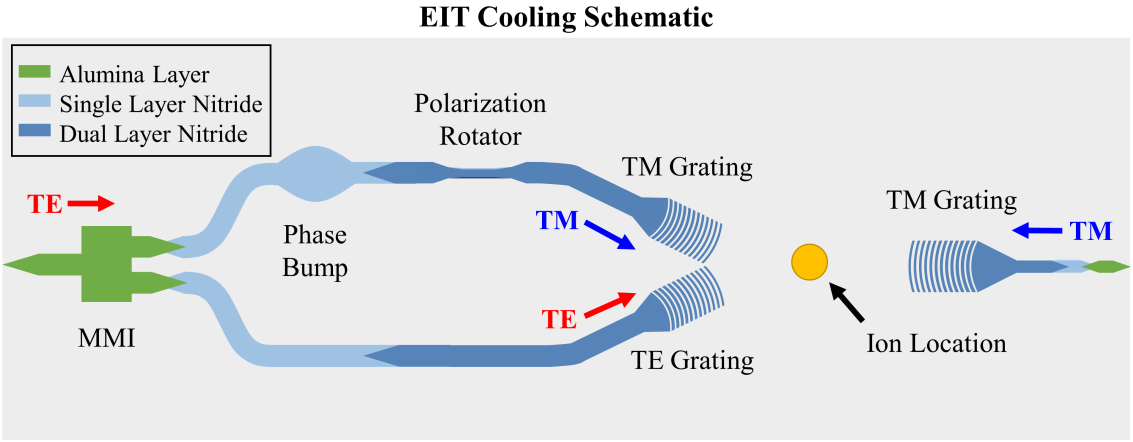

Figure 2.4: Simplified schematics showing the proposed integrated-photonics-based architectures for EIT cooling (not to scale).

edge coupler to an alumina waveguide. Next, the light is split evenly into two arms using a 32.2-µm-long 1x2 alumina multi-mode interferometer (MMI) [14]; simulated efficiency as a function of device length for the MMI is shown in Fig. 2.5a. In the upper arm, the light is transitioned to single-layer silicon nitride. Then, the waveguide is adiabatically widened for a given length, forming a phase bump to impart a 90° phase shift [15]; simulated phase as a function of bump width is shown in Fig. 2.5b. After passing through the phase bump, the light is transitioned to dual-layer nitride. There, it goes through an off-axis polarization rotator, which rotates the incoming light from TE to TM (introduced in detail in Chapter 3); the conversion efficiency as a function of device length can be seen in Fig. 2.5c, with a peak simulated conversion efficiency of 99.15% [16]. More information on the design and experimental results of polarization control devices for PG and EIT cooling can be found in Chapter 3. Finally, the TM light in the upper arm is emitted via a TM grating. In the lower arm from the MMI, the TE light is transitioned to dual-layer nitride and is emitted via a TE grating. The two gratings in each arm are angled so that the beams combine and form approximately circularly polarized light at the ion location. The linear TM input is coupled on-chip from an inverse-taper edge coupler into an alumina waveguide. Next, it is transitioned to dual-layer silicon nitride, where it emits from a focusing TM grating placed opposite to the circularly polarized source, thus enabling EIT cooling.

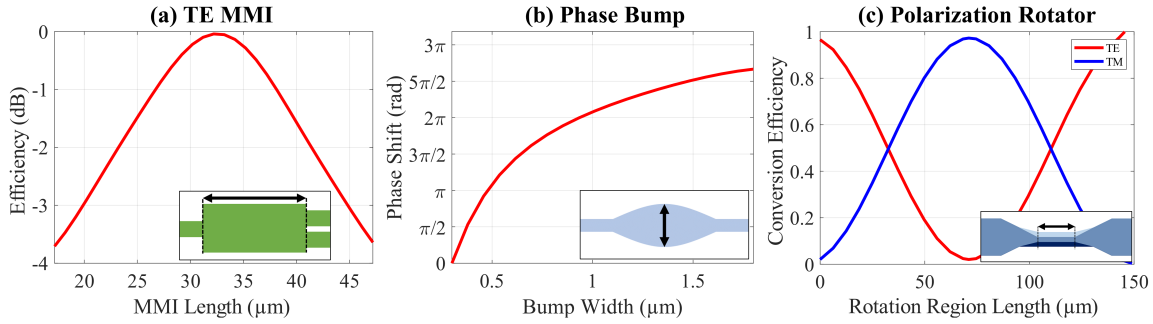

Figure 2.5: (a) Simulated MMI efficiency as a function of MMI length (inset shows device schematic). (b) Simulated phase delay as a function of phase bump width (inset shows device schematic). (c) Simulated conversion efficiency of the off-axis polarization rotator with TE in red and TM in blue (inset shows device schematic).

2.3 Conclusion

In this chapter, we have developed a framework for two advanced trapped-ion cooling schemes, PG and EIT, using a visible-wavelength silicon-photonics platform at 422 nm. We have also developed designs of key integrated-photonics components required to realize these architectures. This approach provides a scalable platform that promises more rapid cooling of multiple vibrational modes when compared to previously shown integrated approaches. Additionally, these approaches should be applicable to neutral-atom laser cooling when tailored to other wavelengths.

Chapter 3

Integrated Visible-Light Polarization Rotators and Splitters for Atomic Quantum Systems

The following work was done in collaboration with Tal Sneh (MIT), Milica Notaros (MIT), Sabrina Corsetti (MIT), Patrick T. Callahan (Lincoln Laboratory), John Chiaverini (Lincoln Laboratory), and Jelena Notaros (MIT). This work has been published in [17].

3.1 Introduction

Polarization control plays an important role in silicon-photonics systems, as it enhances functionality on chip, such as increased channel density for communications and improved performance for polarization-sensitive devices [18, 19]. For this reason, extensive research has been devoted to the development of integrated polarization-control devices, namely, polarization rotators and splitters. Polarization splitters are a vital component for separating or combining polarizations on chip; in prior work, integrated polarization splitters have been demonstrated using mode-evolution devices [20], asymmetric directional couplers [21, 22], higher-order-mode-assisted directional couplers [23], multi-mode interferometers [24], and asymmetric Mach-Zehnder

interferometers [25]. Polarization rotators, another vital component for polarization diversity, enable rotation from an input polarization to an orthogonal output polarization; in prior work, integrated polarization rotators have been demonstrated using mode evolution [19], adiabatic mode conversion [23, 26], and mode coupling devices [27,28]. Additionally, the combination of the two has also been demonstrated in integrated rotator-splitter configurations, which consist of splitting orthogonal polarizations and rotating one polarization to match the other [29–31].

However, most demonstrations of integrated polarization-control devices have been limited to telecom wavelengths. Nevertheless, the recent emergence of integrated-photonics technologies at visible wavelengths opens an entirely new field for polarization control. For example, applications such as underwater communications, quantum networks, and atomic technologies greatly benefit from the reduced size and complexity of integrated photonics [2, 3, 32–34] but require polarization diversity at visible wavelengths. In particular, atomic technologies benefit from the scalability and inherent stability of integrated photonics [2, 3, 35, 36]; polarization-control devices would greatly enhance on-chip functionality for atomic systems, such as advanced cooling schemes for trapped ions [13] or polarization-sensitive operations for neutral atoms [23,35,36]. However, polarization-control devices are difficult to realize at visible wavelengths due to device scaling with wavelength, as moving to shorter wavelengths causes device size to shrink, resulting in feature sizes that approach the limits of fabrication capabilities.

In this work, we design and experimentally demonstrate the first integrated polarization splitters and rotators at blue wavelengths. We design and fabricate for the challenging wavelength of 422 nm, an important transition for $^{88}Sr^{+}$ ions. To realize visible-wavelength polarization diversity, the polarization splitter uses an asymmetric-directional-coupler design to split the polarizations efficiently and compactly. The polarization rotator uses a mode-coupling design, which has the advantage of being able to rotate the polarization in a compact length. Next, these devices are fabricated using the MIT Lincoln Laboratory 200-mm wafer-scale process for trapped-ion applications, consisting of one layer of alumina and two layers of silicon nitride with

a silicon-dioxide cladding. Finally, the performance of the devices is experimentally demonstrated, resulting in a measured polarization-splitter transverse-electric (TE) thru-port coupling of 98.0% and transverse-magnetic (TM) tap-port coupling of 77.6% for a compact length of 16 µm, and a polarization-rotator conversion efficiency of 92.2% for a compact length of 111 µm. This work paves the way for more sophisticated integrated control of trapped-ion and neutral-atom quantum systems.

3.2 Polarization Splitter Design

The devices in this work were designed for compatibility with the MIT Lincoln Laboratory 200-mm wafer-scale fabrication process for wavelengths spanning from ultraviolet to near infrared for trapped-ion applications [10]. The stack consists of a 100-nm-thick alumina layer and two 100-nm-thick silicon-nitride layers separated by 90 nm of silicon dioxide. The devices were designed for an operating wavelength of 422 nm to target the $S_{1/2}$ to $P_{1/2}$ transition of $^{88}Sr^{+}$, a commonly used species for trapped-ion qubits. While these devices were specifically designed for 422 nm, the designs in this work are easily extendable to any wavelength of interest for both trapped ions and neutral atoms.

First, we design an integrated polarization splitter, which splits orthogonal polarizations from a single waveguide into two separate output ports. Specifically, we use an asymmetric directional coupler scheme due to its compact length [21, 22]. An asymmetric directional coupler typically consists of one regular rectangular waveguide and a second unconventional waveguide that breaks the symmetry of the system, such as a sub-wavelength-grating waveguide or a nano-slot waveguide [21,22]. By correctly tuning the geometric parameters, the effective indices of the thru and tap waveguides can be matched for one polarization but not the other, allowing power transfer to only occur for one polarization.

Here, we use the two layers of nitride available in our platform to generate the asymmetry that enables polarization splitting. We design the thru-port waveguide to be a standard rectangular waveguide in a single layer of nitride and the tap-port

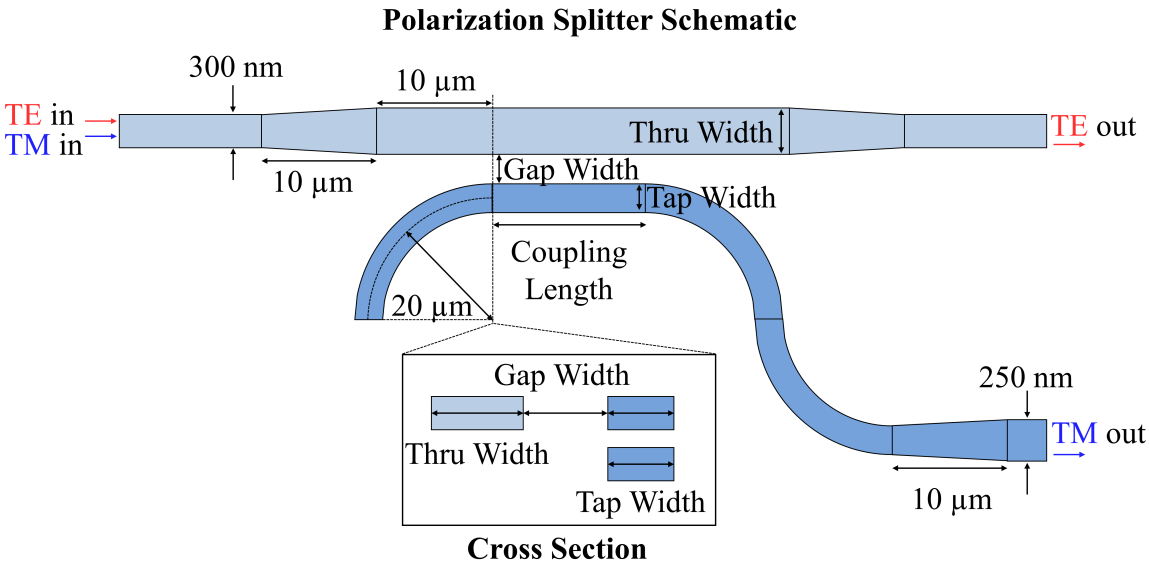

Figure 3.1: Integrated polarization splitter device schematic and cross section (not to scale), showing critical dimensions for polarization splitting.

waveguide to be a dual-layer waveguide consisting of two vertically-stacked nitride layers. Fig. 3.1a shows the geometry of the polarization splitter, with the single-layer and dual-layer nitride waveguides placed side-by-side with a gap of 200 nm. By changing the widths of the tap and thru waveguides, the effective indices can be matched for the TM mode, but not the TE mode (Fig. 3.2). Fig. 3.3 shows the difference between the effective indices of the thru and tap waveguides for both the TM and TE polarizations (simulated using Lumerical MODE). Using these plots, we can choose the tap and thru waveguide widths such that the difference in the effective indices is minimized for the TM polarization. Here, we choose a single-layer nitride waveguide width of 370 nm and a dual-layer nitride waveguide width of 200 nm, with a gap between the two waveguides of 200 nm, such that we achieve a balance between the resulting required coupling length while maintaining reasonable dimensions for fabrication. This yields a Δn_{eff} of 0.0012 for TM and a larger Δn_{eff} of 0.0355 for TE, enabling strong coupling between the thru and tap waveguides for only the TM mode.

Next, for the chosen device cross section, we choose the optimal coupling length for full power transfer. Fig. 3.4 shows the transmission for both the TE and TM modes

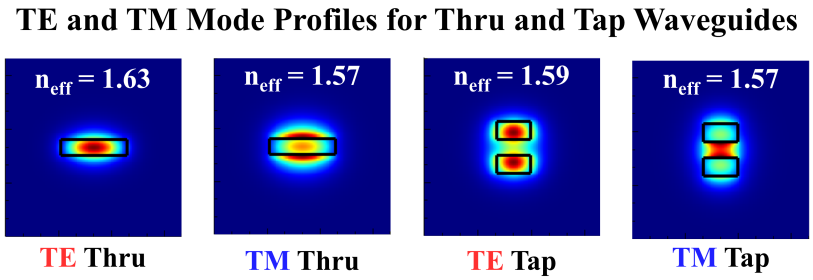

Figure 3.2: Simulated TE and TM mode profiles for the thru and tap waveguides, showing mode effective index matching for the TM modes but not the TE modes.

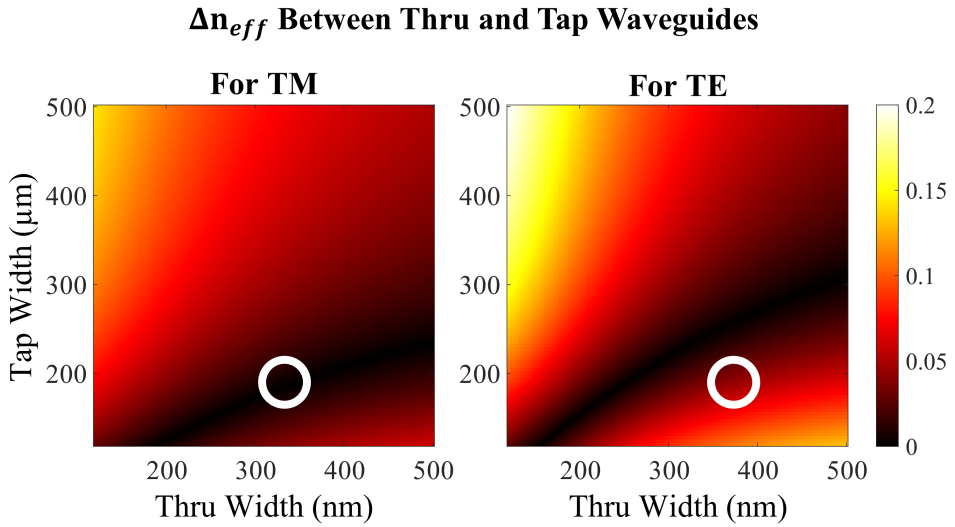

Figure 3.3: Simulated difference in effective indices between the thru and the tap waveguide modes as a function of the tap and thru waveguide widths for the TM (left) and TE (right) polarizations (with white circles marking the chosen operating point).

in the thru and tap ports as a function of coupling length (simulated using Lumerical FDTD). Note that bends are included in the design to bring the waveguides into and out of the interaction region, as shown in Fig. 3.1. A coupling length of 16 μm gives peak power transfer for a 370-nm-wide thru waveguide, 200-nm-wide tap waveguide, and 200-nm gap. The peak power transfer efficiency from the thru to tap port of the TM mode is 98.6%. The TE power transfer to the tap port remains minimal at the designed coupling length, with a low 1.1% coupling to the tap port.

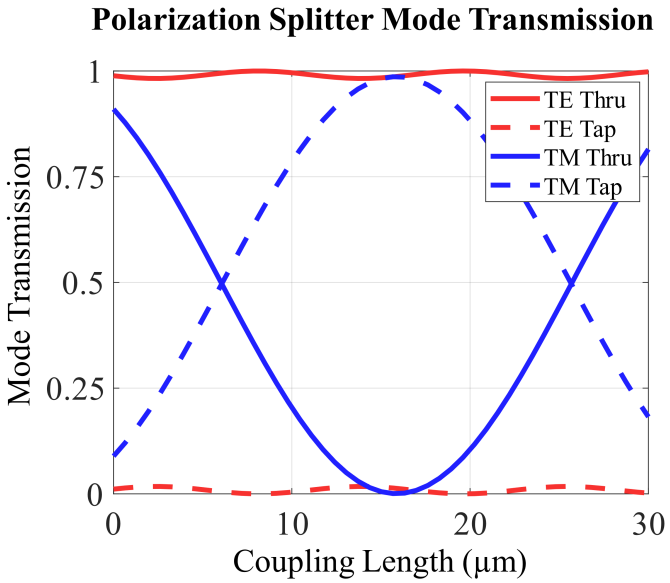

Figure 3.4: Simulated TE (red) and TM (blue) mode transmission as a function of coupling length for a polarization splitter with 370-nm-thru width and a 200-nm-tap width.

3.3 Polarization Rotator Designs

3.3.1 Off-Axis Polarization Rotator Design

Second, we design an integrated polarization rotator. Specifically, we use a mode-coupling polarization rotator scheme (also called an off-axis polarization rotator in this work) due to its ability to rotate polarizations within short lengths [27, 28]. In a mode-coupling polarization rotator, an asymmetric index profile creates supported orthogonal eigenmodes with polarization axes at ± 45 degrees with respect to the substrate [27,28]. Therefore, incident light with either TE- or TM-polarization excites both eigenmodes equally. An interaction length that induces a π phase shift between the two eigenmodes will then cause a 90° rotation of the input polarization [27, 28].

Here, we leverage the two layers of nitride in our platform, combined with a lateral offset between layers, to create the asymmetric index profile needed to induce polarization rotation (Fig. 3.6). Fig. 3.6b shows, as a function of waveguide width and offset, the fraction of TE polarization in the rotation region, defined as the TE polarization fraction (simulated using Lumerical MODE). A TE polarization fraction

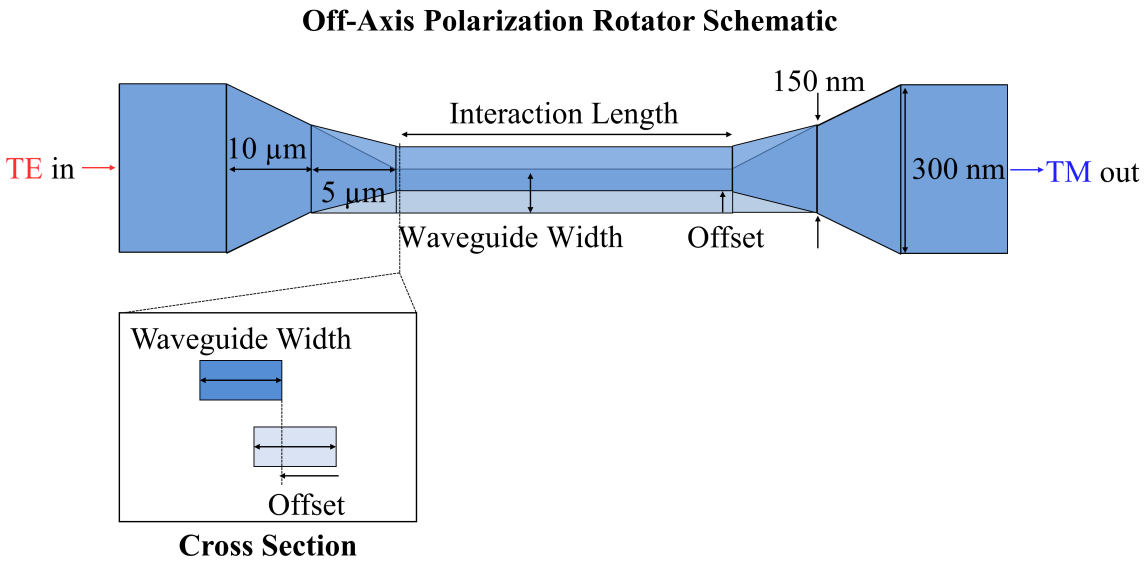

Figure 3.5: Integrated off-axis polarization rotator device schematic and cross section (not to scale), showing critical dimensions for polarization rotation.

of 50% creates the two orthogonal eigenmodes desired for rotation. The plot shows that, for this short wavelength, small feature sizes are needed to achieve polarization rotation, making design of these polarization rotators at visible wavelengths a challenge. A waveguide width of 110 nm for both layers and an 85-nm lateral offset is chosen to yield a TE polarization fraction of 50%.

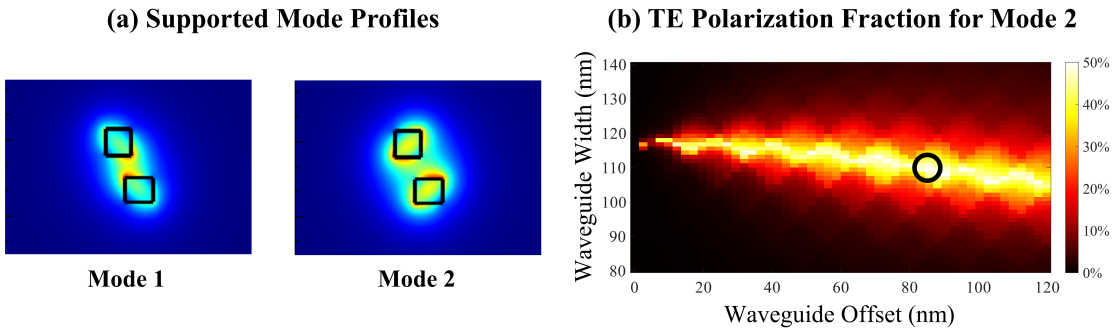

Figure 3.6: (a) Simulated mode profiles for the two ±45° polarized eigenmodes in the interaction region. (b) Simulated TE polarization fraction for the second supported mode as a function of waveguide width and offset (with white circles marking the chosen operating point).

To excite the eigenmodes equally in the rotation region, the transition into the rotation region must be abrupt. However, abrupt transitions cause reflection loss.

Tapers can be introduced to decrease the reflection loss; however, the length of the tapers must be short enough that they do not adiabatically transform the input mode, as this will, in general, lead to unequal excitation of the two modes. Here, taper lengths of 5 µm are chosen to balance reflection losses from abrupt transitions without adiabatically transforming the mode. Next, for the chosen device cross section and taper length, we determine the optimal interaction region length. Fig. 3.7 shows a sweep of the interaction region length for the designed waveguide width and offset (simulated using Lumerical FDTD). An interaction region length of 71 µm gives the peak polarization conversion for a device with 110-nm waveguides and an 85-nm offset. Including the tapers, the total device length is 111 µm and yields a theoretical TE-to-TM conversion efficiency of 99.2%.

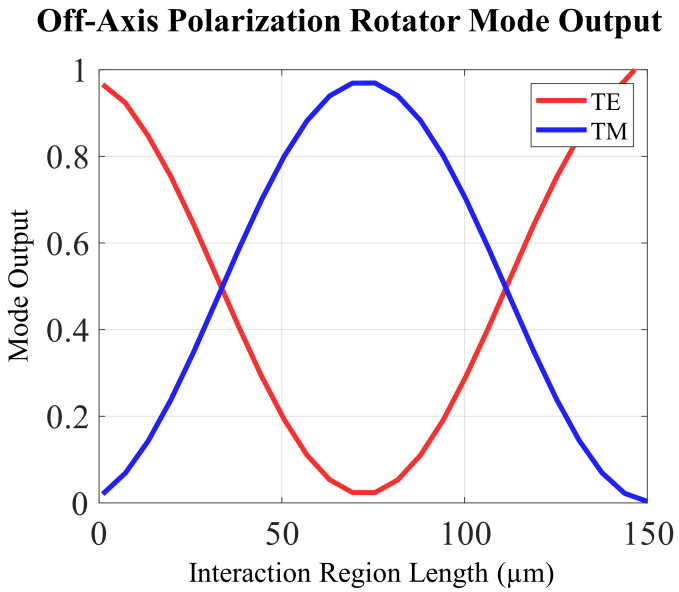

Figure 3.7: Simulated TE (red) and TM (blue) mode outputs with a TE input as a function of interaction region length for a polarization rotator with 110-nm-waveguide width and 85-nm-waveguide offset.

3.3.2 Adiabatic Polarization Rotator Design

Another method for polarization rotation is to use adiabatic mode conversion between the higher-order TE and fundamental TM modes. Adiabatic polarization rotators

have the advantage of being more broadband and fabrication tolerant compared to mode-coupling polarization rotators at the expense of longer lengths [19,23,26,31]. For devices that have a vertically-asymmetric index profile, such as an air cladding or a rib etch, an anti-crossing occurs in the effective index curves as a function of waveguide width between the first higher-order TE mode (TE_{10}) and the fundamental TM mode (TM_{00}) [26]. The modes in this region are hybridized, transforming TE_{10} to TM_{00} as the waveguide width is changed adiabatically. Typically, polarization rotators convert between the two fundamental modes (TE_{00} and TM_{00}), so an asymmetric directional coupler, a higher-order mode converter, or a mode evolution device can first be used to convert the TE_{10} mode to the TE_{00} mode [23, 26, 31].

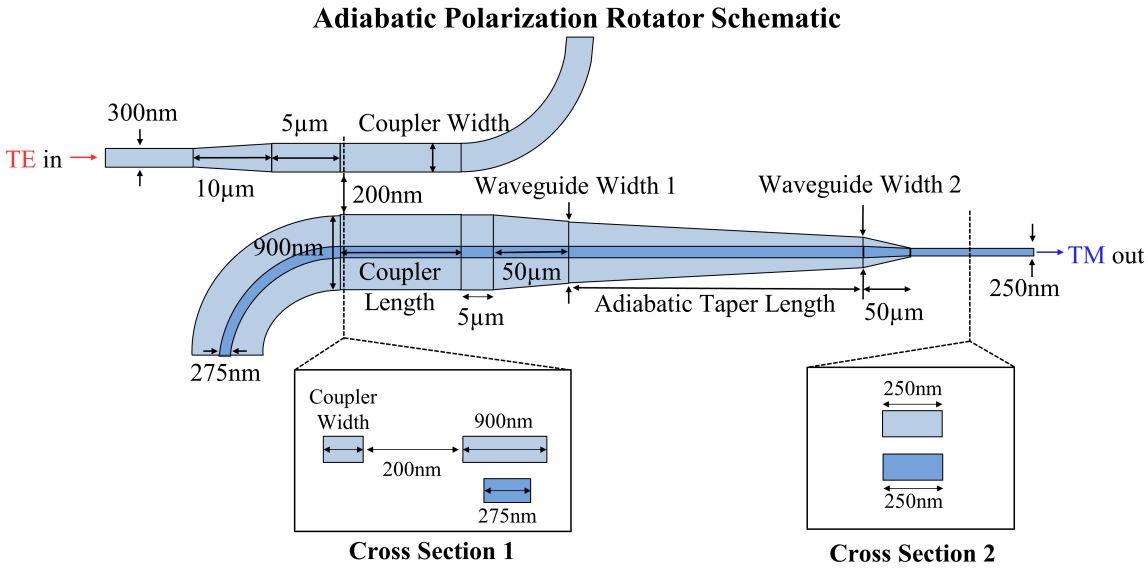

Figure 3.8: Integrated adiabatic polarization rotator device schematic and cross sections (not to scale), showing critical dimensions for polarization rotation.

For this device, for the TE_{00} to TE_{10} conversion, we use an asymmetric directional coupler due to its compact length. Coupling occurs between the two modes when the effective indices of the TE_{00} mode in the thru waveguide and the TE_{10} mode in the tap waveguide match. Fig. 3.10a shows the difference between the effective indices of the TE_{00} mode in the thru waveguide and the TE_{10} mode in the tap waveguide. Using this plot, the waveguide widths for the thru and tap port are chosen to be 408 nm and 900 nm, respectively, to optimize this match. This yields a Δn_{eff} of 0.00011

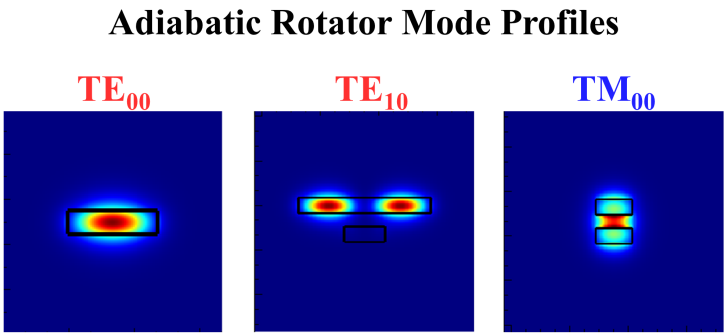

Figure 3.9: Simulated mode profiles for the TE_{00} mode in the thru waveguide of the coupler region, TE_{10} mode in the tap waveguide of the coupler region, and TM_{00} mode at the output of the device.

between the TE_{00} and TE_{10} modes. To determine the optimal coupling length, bends are introduced, and the coupler length is swept. Fig. 3.10b shows a peak coupling of 99.9% at a length of 94.4 µm.

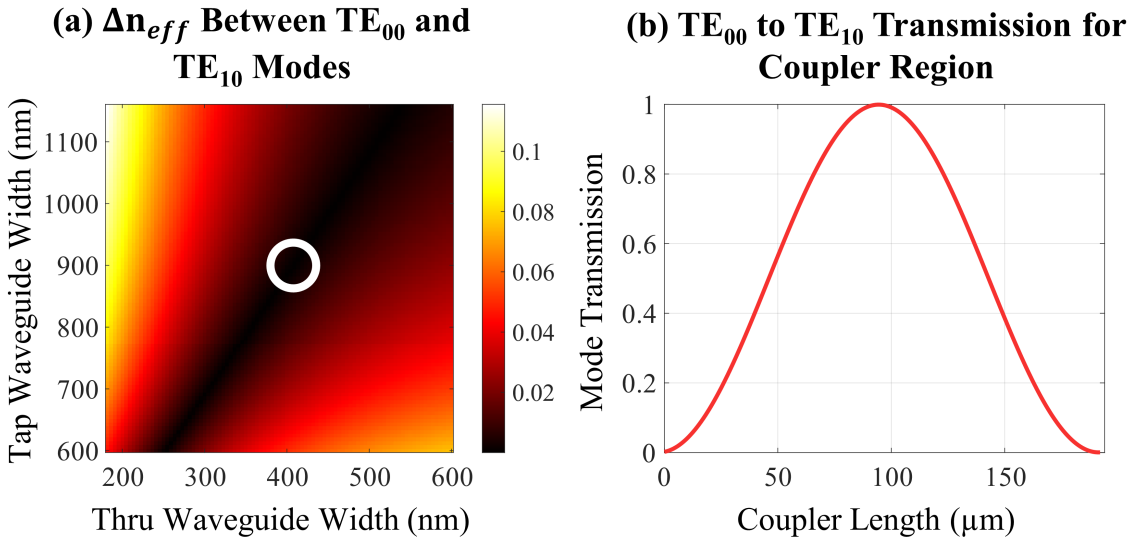

Figure 3.10: (a) Simulated difference in effective indices for the TE_{00} mode in the thru waveguide and the TE_{10} mode in the tap waveguide (with white circle marking the chosen operating point); coupling occurs when the difference approaches zero. (b) Simulated TE_{10}-mode transmission to the thru port as a function of coupling length for the TE_{00} to TE_{10} coupler with thru and tap waveguide widths of 408 nm and 900 nm, respectively.

Next, to convert between the TE_{10} and TM_{00} modes, we generate an asymmetric index profile by introducing a second waveguide above the adiabatic taper region.

Fig. 3.11 shows the effective indices for the TE_{10} and TM_{00} modes as a function of waveguide width. In this device, the anti-crossing where mode hybridization occurs is around a 780-nm waveguide width. By taking advantage of this anti-crossing and varying the waveguide width adiabatically along the length of the taper, the polarization can be rotated. The mode is most sensitive around the anti-crossing and, for this reason, the waveguide width must be changed very slowly around the anti-crossing point. To reach the anti-crossing region, however, shorter tapers on either side of the anti-crossing point can be introduced to convert the mode to the desired spot size, which allows the rotator length to be more compact.

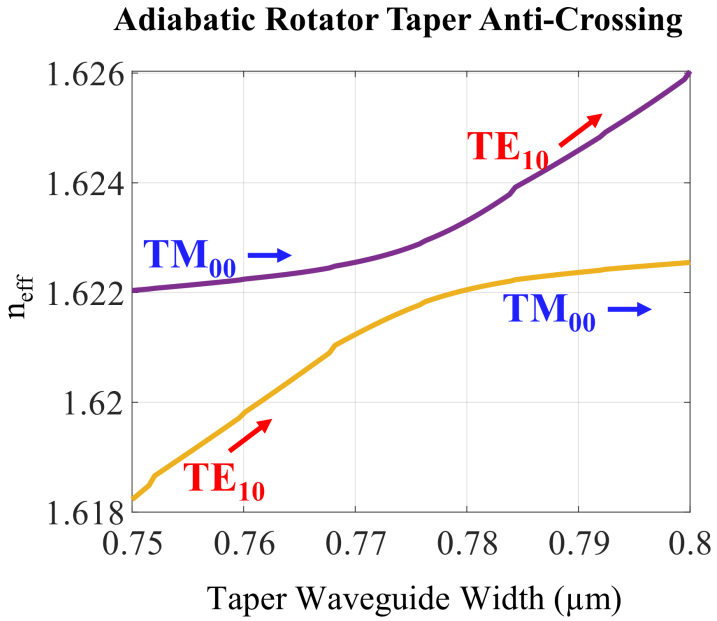

Figure 3.11: Simulated effective index anti-crossing behavior as a function of bottom waveguide width.

Next, the length of the adiabatic taper region is swept, assuming 50-µm-long spot-size converters are used. Fig. 3.12 shows the TE_{10} to TM_{00} conversion efficiency as a function of the adiabatic taper length. Since this is an adiabatic device, longer taper lengths achieve higher conversion efficiencies. An adiabatic taper length of 350 µm is chosen. The final device design consists of a TE_{00} to TE_{10} and a TE_{10} to TM_{00} mode converter, with a simulated conversion efficiency of 93.5% and a total device length of 550µm.

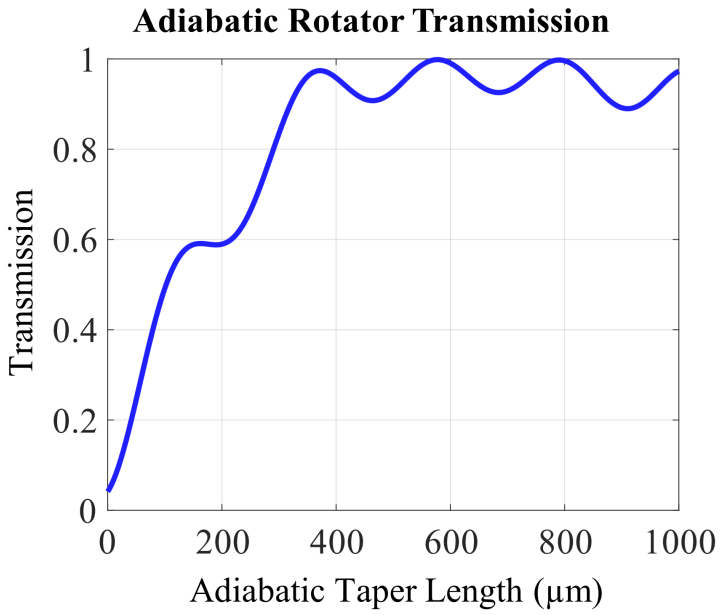

Figure 3.12: Simulated TM_{00}-mode transmission of the adiabatic polarization rotator as a function of adiabatic taper length.

3.4 Polarization Splitter Experimental Results

Next, we fabricated the polarization splitter and the off-axis polarization rotator using the MIT Lincoln Laboratory 200-mm wafer-scale fabrication process for wavelengths spanning from ultraviolet to near infrared for trapped-ion applications, mentioned above. The stack consists of a 100-nm-thick alumina layer and two 100-nm-thick silicon-nitride layers separated by 90 nm of silicon dioxide. Further platform details are provided in [10]. The fabricated polarization splitter can be seen in Fig. 3.13, which show the dark-field micrograph of the fabricated integrated polarization splitter.

First, to characterize the fabricated integrated polarization splitter, we couple 423.4-nm-wavelength light from a laser diode onto the chip using single-mode fiber. We use polarization paddles to tune the input polarization, and we couple light off the chip using a single-mode fiber to an optical detector (Fig. 3.14b). The performance of the device is measured by first setting the input polarization to TE and measuring the optical power in both the thru and tap ports. Then, the input polarization is set

to TM, and both the thru and tap ports are measured again.

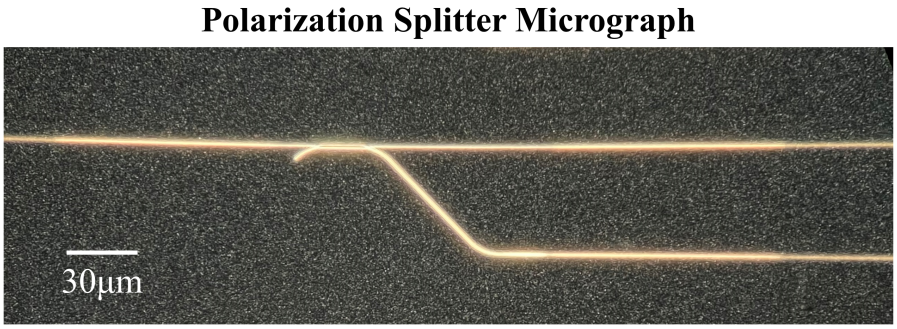

Figure 3.13: Dark-field micrograph of the fabricated integrated polarization splitter.

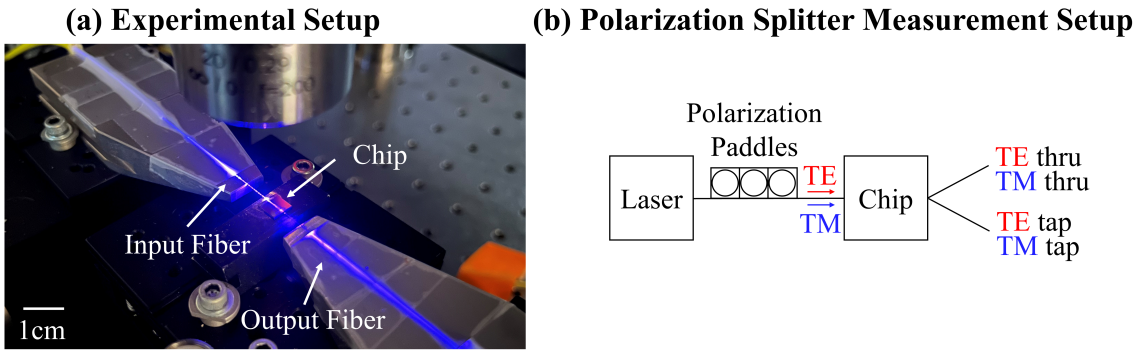

Figure 3.14: (a) Photograph of the measurement setup, consisting of blue laser light from a laser diode coupled on and off the chip using single-mode fibers. (b) Setup diagram for the polarization-splitter measurements.

The performance of the splitter for both polarizations and ports is shown in Fig. 3.15. We fabricated five variations of the device, where the waveguide widths were varied from the nominal design dimensions; both the thru and tap waveguide widths vary by the same amount, while the size of the gap changes with the size of the waveguides. For each variant of the device, we measured the thru and tap ports for both polarizations. For each polarization, we normalize the thru and tap port powers to the total power at the output to account for polarization-dependent losses. The peak TM coupling was measured to be 77.6% to the tap port (and 22.4% to the thru port). The TE coupling was measured to be 98.0% to the thru port (and 2.0% to the tap port). Note that the measurement of the TE extinction of the device was limited

by the local noise floor of the measurement. We attribute the difference between the expected simulated and the experimentally demonstrated TM coupling to fabrication variations.

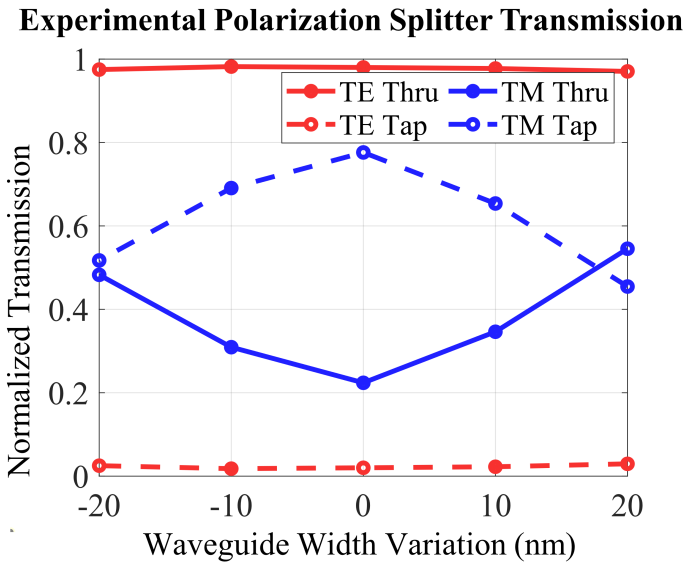

Figure 3.15: Experimental polarization-splitter transmission into the thru and tap ports for TE (red) and TM (blue) polarization as a function of waveguide width variation.

This device demonstrates successful splitting, with a TM coupling of 77.6% to the tap port, with a minimal TE coupling of 2.0% to the tap port, for a compact length of only 16 µm. This result represents the first demonstration of an integrated polarization splitter at blue wavelengths.

3.5 Off-Axis Polarization Rotator Experimental Results

Second, to characterize the fabricated integrated off-axis polarization rotator (Fig. 3.16), we use an experimental setup with a very similar configuration to the setup described in Section 3.4, with a few modifications. On the output, the output fiber is connected to a fiber-based polarizing beam splitter (PBS), which splits the polarizations of the incoming light into two orthogonal outputs (Fig. 3.17). Additionally,

polarization paddles are used on the output to align the on-chip TE and TM axes to the PBS axes. To measure the device, first, the input polarization is set to TE using a polarization-sensitive grating emitter. Then, light is coupled on and off the chip through a straight waveguide, and the outcoupled TE light is used to align the output polarization paddles to the axes of the PBS. Then, the performance of the on-chip rotator is measured by inputting TE light into the device and recording the measured optical power outputs at the TE and TM ports of the PBS.

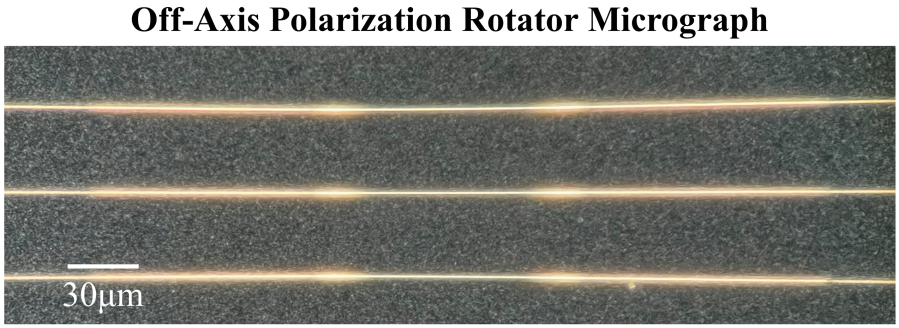

Figure 3.16: Dark-field micrograph of the fabricated integrated off-axis polarization rotator.

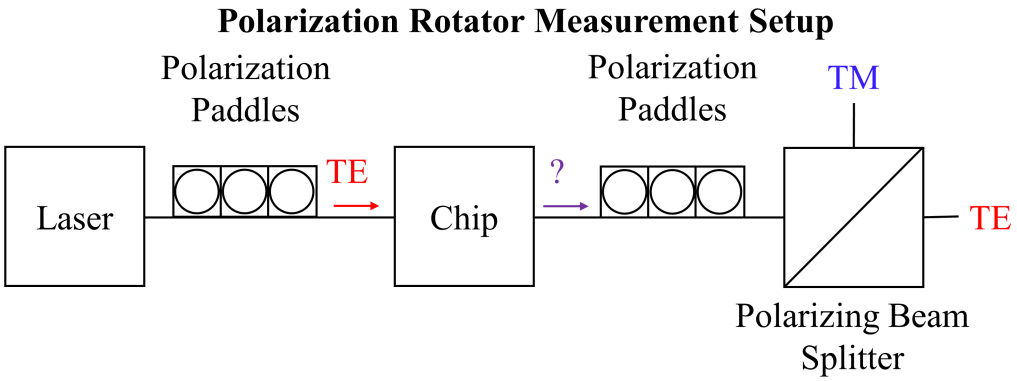

Figure 3.17: Setup diagram for the polarization-rotator measurements.

The performance of the polarization rotator is shown in Fig. 3.18. Fig. 3.18a shows the power in the TE and TM polarizations at the output of the device as a function of waveguide width (six variations of the device were fabricated with waveguide widths varied from the nominal design). We observe power transfer between the

two polarizations, with a peak power transfer from the TE input mode into the TM output mode at a waveguide width of 120 nm. Fig. 3.18b shows the TE-to-TM conversion efficiency of the device, defined as the ratio of TM power to the total power in the device, as a function of waveguide width. The measured peak conversion efficiency of the device is 92.2%. Additionally, the insertion loss through the device is measured using a separate suite of loss structures, and the total transmission is found to be greater than 95%.

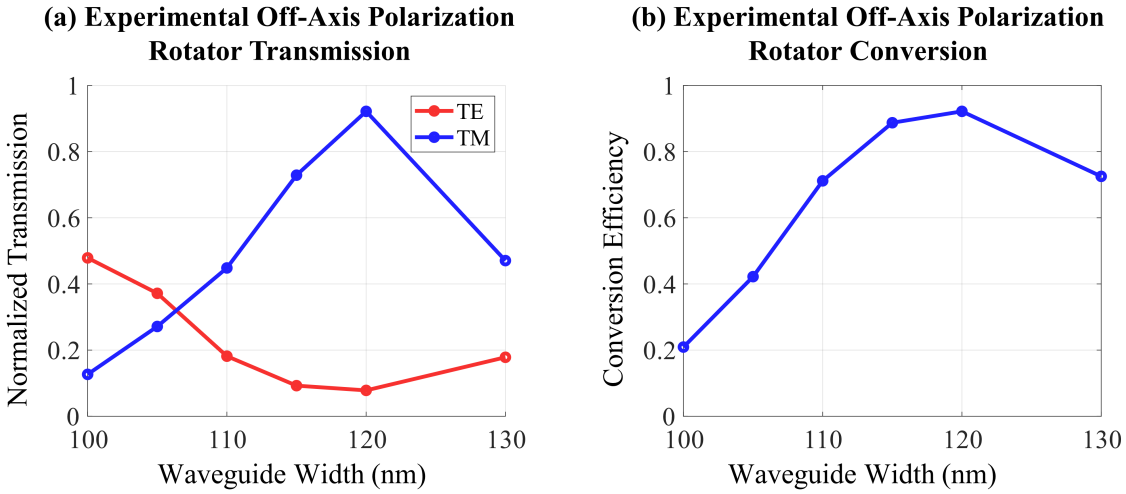

Figure 3.18: (a) Experimental polarization-rotator TE (red) and TM (blue) output with a TE input as a function of waveguide width. (b) Experimental polarization-rotator TE-to-TM conversion efficiency as a function of waveguide width.

Peak performance occurs for a 111-µm-long device with 110-nm waveguides and an 85-nm offset with a measured conversion efficiency of 92.2%. This result represents the first demonstration of an integrated polarization rotator at blue wavelengths.

3.6 Conclusion

In summary, we have shown the design and experimental demonstration of the first integrated polarization splitters and rotators at blue wavelengths. We designed and fabricated for the challenging wavelength of 422 nm, an important transition for $^{88}Sr^{+}$ ions. The design of the polarization splitter consists of an asymmetric-directional-coupler design to split the polarizations efficiently and compactly. The design of the

polarization rotator uses a mode-coupling design, which rotates the polarization in a compact length. The devices were then fabricated using the MIT Lincoln Laboratory 200-mm wafer-scale process for trapped-ion applications, consisting of one layer of alumina and two layers of silicon nitride with a silicon-dioxide cladding. Finally, the performance of the devices was experimentally demonstrated, resulting in a measured polarization-splitter TE thru-port coupling of 98.0% and TM tap-port coupling of 77.6% for a compact length of 16 µm, and a polarization-rotator conversion efficiency of 92.2% for a compact length of 111 µm.

These blue-wavelength polarization-control devices enable visible-wavelength polarization diversity for the important application of integrated optical control of atomic systems [13, 23, 35, 36]. For example, to demonstrate enhanced laser cooling of trapped-ion systems, we are using these polarization devices to enable future integrated-photonics-based polarization-gradient and electromagnetically-induced-transparency cooling systems for trapped $^{88}Sr^{+}$ ions [13]. While these devices were specifically designed for compatibility with $^{88}Sr^{+}$ ions, the designs and methodology described in this work are easily extendable to any wavelength of interest for both trapped ions and neutral atoms. The polarization-control devices introduced by this work pave the way for more sophisticated integrated control of atomic quantum technologies.

Chapter 4

Integrated Polarization-Diverse Grating Emitters for Trapped-Ion Systems

The following work was led by Sabrina Corsetti (MIT) and done in collaboration with Reuel Swint (MIT Lincoln Laboratory), Milica Notaros (MIT), Gavin N. West (MIT), Tal Sneh (MIT), Felix Knollmann (MIT), Patrick T. Callahan (MIT Lincoln Laboratory), Thomas Mahony (MIT Lincoln Laboratory), Ethan R. Clements (MIT), Cheryl Sorace-Agaskar (MIT Lincoln Laboratory), Dave Kharas (MIT Lincoln Laboratory), Robert McConnell (MIT Lincoln Laboratory), John Chiaverini (MIT Lincoln Laboratory), and Jelena Notaros (MIT). This work has been published in [37].

4.1 Introduction

As discussed in Chapter 2, systems of trapped ions are a promising modality for quantum information processing due to their long coherence times and strong ion-ion interactions, which enable high-fidelity two-qubit gates [1]. However, most current implementations are comprised of complex free-space optical systems, whose large size and susceptibility to vibrations and drift can limit fidelity and addressability of ion arrays, hindering scaling to large numbers of qubits. Recently, integrated-photonics-

based devices and systems have been demonstrated as an avenue to address these challenges [3].

To date, these prior integrated demonstrations have been limited to operations using light of only a single linear polarization, specifically transverse electric (TE), nominally parallel to the ion-trap chip surface. However, diverse polarizations are critical for enabling numerous operations for advanced trapped-ion systems, leading to an interest in developing polarization-diverse emitters [4,38]. For example, integrated-photonics-based architectures involving light of both TE and transverse-magnetic (TM) polarizations (such as the configuration in Fig. 2.1) are necessary for enabling advanced ion cooling schemes that offer sub-Doppler temperatures over several non-degenerate trap-vibrational modes, such as polarization-gradient and electromagnetically-induced-transparency cooling, as discussed in Chapter 2 [13].

In this section, we design and experimentally demonstrate a pair of integrated TE- and TM-emitting gratings with an operating wavelength of 422 nm, corresponding to the $5^2S_{1/2}$ to $5^2P_{1/2}$ transition of $^{88}Sr^+$ ions, a key transition for ion control. We implement a custom optimization-based design algorithm to realize bilayer, apodized, and curved gratings that emit unidirectional focused beams, with experimentally measured spot dimensions of 7.6 µm by 4.3 µm for the TE grating and 5.0 µm by 3.6 µm for the TM grating at a target ion height of 50 µm above the surface of the chip. This work represents, to the best of our knowledge, the first development of integrated TM-emitting gratings for trapped-ion systems, and, thus, a fundamental stepping stone on the path to advanced operations for integrated-photonics-based trapped-ion quantum systems involving multiple polarizations.

4.2 Grating Design Process and Simulation Results

Both of the gratings in this section are comprised of two 100-nm-thick layers of silicon nitride separated by 90 nm of silicon dioxide, with the grating teeth fully etched into the nitride. The pitch and duty cycles of each layer's grating teeth are optimized such that the gratings emit focused beam profiles that maximize the percentage of light

emitted towards a target ion location 50 µm above the surface of the chip. In addition, the teeth in each layer are offset from each other in the propagation dimension (x) to enable unidirectional emission upwards [39]. Finally, the grating teeth are curved to enable focusing in the transverse dimension (y) of the grating.

To design each grating, we utilize a particle swarm algorithm to determine the optimal pitches, duty cycles, and offsets of the teeth in both layers. Then, we use a slab mode simulation to determine the optimal grating tooth curvature, based on the phase front of the mode propagating in the grating. Finally, we simulate the grating and compute its expected emission angle, beam dimensions, and efficiency.

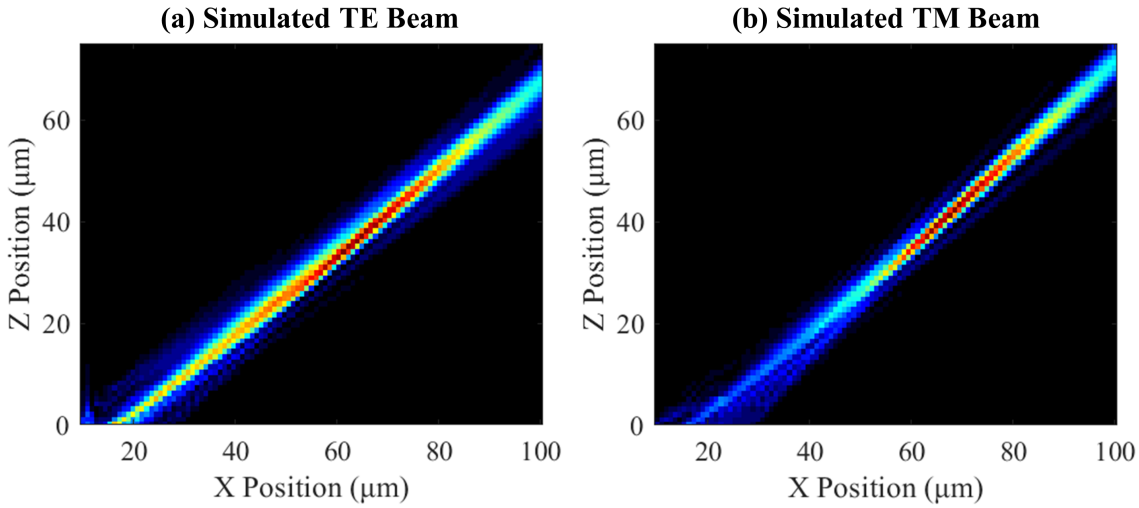

Figure 4.1: Simulated xz intensity profiles for the (a) TE and (b) TM grating.

The gratings developed in this work are designed with a 17 µm by 18 µm emitting aperture area. This size was chosen such that the optimized TE and TM gratings emit with matching efficiencies – a necessary condition for many ion operations involving both polarizations, such as polarization-gradient cooling [13]. The resulting simulated emission profiles in the xz plane for both gratings are plotted in Fig. 4.1a–b. The TE grating has an expected emission angle of 48.6° and a spot size ($1/e^2$ diameter) of 9.9 µm by 5.0 µm at the ion location 50 µm above the chip surface. The TM grating has an expected emission angle of 47.8° and a spot size of 6.1 µm by 3.7 µm at the ion location 50 µm above the chip surface.

4.3 Grating Fabrication and Experimental Results

The designed gratings were fabricated in our 200-mm wafer-scale fabrication process developed at MIT Lincoln Laboratory for wavelengths spanning the range from ultraviolet to near infrared (Fig. 4.2) [10].

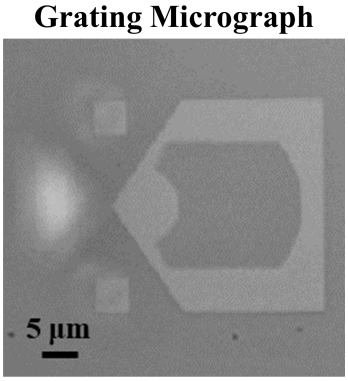

Figure 4.2: Micrograph of a fabricated grating.

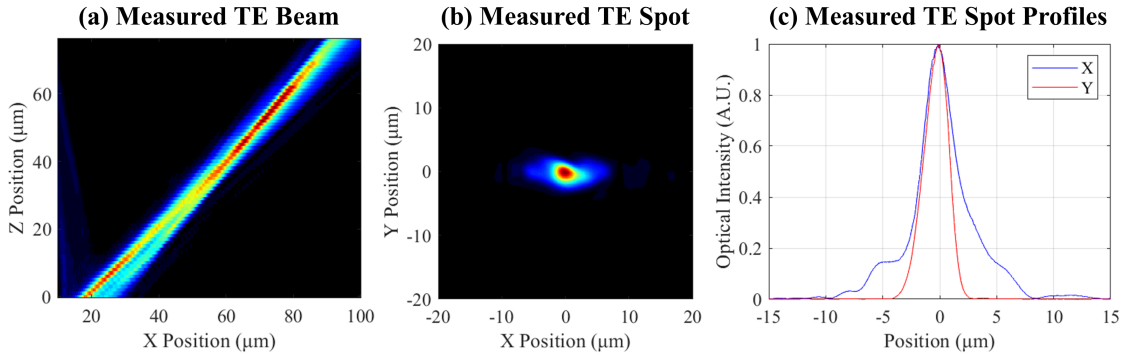

Figure 4.3: (a) Experimentally measured xz intensity profiles for the TE grating. (b) Measured spots in the xy plane at z = 50 µm for the TE grating. (c) Measured spot profiles in the x (blue) and y (red) dimension at z = 50 µm for the TE grating.

To characterize the gratings, light is routed to the chip from a benchtop laser source through a series of polarization-maintaining fibers. At the chip facet, we use a polarizing beam-splitter cube on a mount aligned with the axes of the chip to align the incident polarization of the fiber to the operating polarization of the measured grating (either TE or TM). The light from the fiber is then coupled onto the chip using an on-chip tapered edge coupler, and light is routed to the gratings using a combination

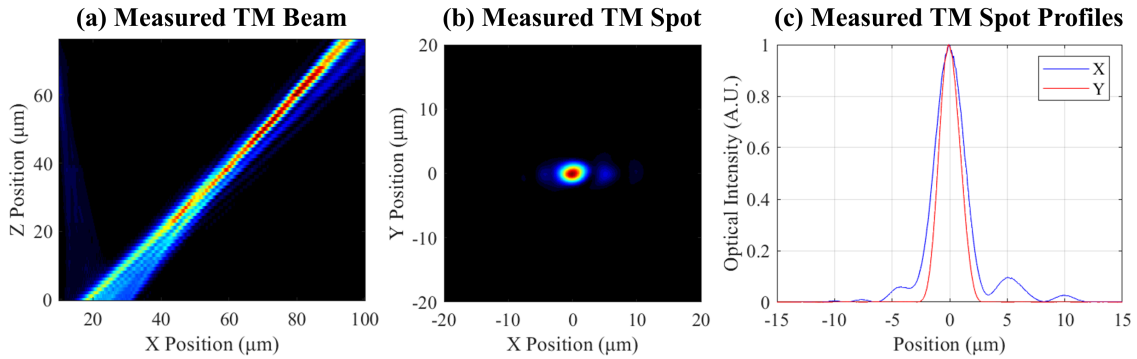

Figure 4.4: (a) Experimentally measured xz intensity profiles for the TM grating. (b) Measured spots in the xy plane at z = 50 µm for the TM grating. (c) Measured spot profiles in the x (blue) and y (red) dimension at z = 50 µm for the TM grating.

of alumina waveguides, silicon-nitride waveguides, and vertical transitions between layers [10]. To measure each grating's performance, we visualize the chip with a 50X objective and a visible-light camera, and use an automated setup to increment the height of the optical train in 1-µm steps to capture images of the grating's emitted beam over a range of 0 to 100 µm above the surface of the chip (Fig. 4.3a, 4.4a). We then use the resulting data to compute the grating's emission angle and beam dimensions (Fig. 4.3b–c, 4.4b–c).

Using this characterization procedure, we find that the fabricated TE grating successfully emits TE-polarized light at an angle of 43.2° (Fig. 4.3a) with a spot size ($1/e^2$ diameter) of 7.6 µm by 4.3 µm at 50 µm above the chip (Fig. 4.3b–c). Similarly, the fabricated TM grating successfully emits TM-polarized light at an angle of 43.1° (Fig. 4.4a) with a spot size of 5.0 µm by 3.6 µm at 50 µm above the chip surface (Fig. 4.4b–c).

4.4 Conclusions

In this section, we designed and experimentally demonstrated a pair of integrated TE- and TM-emitting gratings with an operating wavelength of 422 nm, corresponding to the $5^2S_{1/2}$ to $5^2P_{1/2}$ transition of $^{88}Sr^+$ ions. This work represents, to the best of our knowledge, the first development of integrated TM-emitting gratings for

trapped-ion systems, and, thus, a fundamental stepping stone on the path to advanced operations for trapped-ion quantum systems involving multiple polarizations, such as polarization-gradient and electromagnetically-induced-transparency cooling [13, 16], using an integrated photonics platform.

Chapter 5

Conclusion

5.1 Conclusion

This thesis outlined the key devices and architectures that enable advanced integrated-photonics-based cooling systems for trapped ions.

In Chapter 2, we developed a framework for two advanced trapped-ion cooling schemes, PG and EIT, using a visible-wavelength silicon-photonics platform at 422 nm. We have also presented designs of key integrated-photonics components required to realize these architectures. This approach provides a scalable platform that promises more rapid cooling of multiple vibrational modes when compared to previously shown integrated approaches. Additionally, these approaches should be applicable to neutral-atom laser cooling when tailored to other wavelengths.

Next, in Chapter 3, we showed the design and experimental demonstration of the first integrated polarization splitters and rotators at blue wavelengths. We designed and fabricated for the challenging wavelength of 422 nm, an important transition for $^{88}Sr^{+}$ ions. The design of the polarization splitter consists of an asymmetric-directional-coupler design to split the polarizations efficiently and compactly. The design of the polarization rotator uses a mode-coupling design, which rotates the polarization in a compact length, The performance of the devices was experimentally demonstrated, resulting in a measured polarization-splitter TE thru-port coupling of 98.0% and TM tap-port coupling of 77.6% for a compact length of 16 µm and a

polarization-rotator conversion efficiency of 92.2% for a compact length of 111 µm. While these devices were specifically designed for compatibility with $^{88}Sr^{+}$ ions, the designs and methodology described in this work are easily extendable to any wavelength of interest for both trapped ions and neutral atoms. The polarization-control devices introduced by this work pave the way for more sophisticated integrated control of atomic quantum technologies.

Finally, in Chapter 4, we designed and experimentally demonstrated a pair of integrated TE- and TM-emitting gratings with an operating wavelength of 422 nm. This work represents, to the best of our knowledge, the first development of integrated TM-emitting gratings for trapped-ion systems, and, thus, a fundamental stepping stone on the path to advanced operations for trapped-ion quantum systems involving multiple polarizations, such as polarization-gradient and electromagnetically-induced-transparency cooling, using an integrated photonics platform.

Bibliography

[1] C. D. Bruzewicz, J. Chiaverini, R. McConnell, and J. M. Sage, "Trapped-Ion Quantum Computing: Progress and Challenges," *Applied Physics Reviews*, vol. 6, p. 021314, June 2019. arXiv:1904.04178 [physics, physics:quant-ph].

[2] R. J. Niffenegger, J. Stuart, C. Sorace-Agaskar, D. Kharas, S. Bramhavar, C. D. Bruzewicz, W. Loh, R. T. Maxson, R. McConnell, D. Reens, G. N. West, J. M. Sage, and J. Chiaverini, "Integrated multi-wavelength control of an ion qubit," *Nature*, vol. 586, pp. 538–542, Oct. 2020. Number: 7830 Publisher: Nature Publishing Group.

[3] K. K. Mehta, C. Zhang, M. Malinowski, T.-L. Nguyen, M. Stadler, and J. P. Home, "Integrated optical multi-ion quantum logic," *Nature*, vol. 586, pp. 533–537, Oct. 2020. Number: 7830 Publisher: Nature Publishing Group.

[4] L. Massai, T. Schatteburg, J. P. Home, and K. K. Mehta, "Pure circularly polarized light emission from waveguide microring resonators," *Applied Physics Letters*, vol. 121, p. 121101, Sept. 2022.

[5] G. Moody, V. J. Sorger, D. J. Blumenthal, P. W. Juodawlkis, W. Loh, C. Sorace-Agaskar, A. E. Jones, K. C. Balram, J. C. F. Matthews, A. Laing, M. Davanco, L. Chang, J. E. Bowers, N. Quack, C. Galland, I. Aharonovich, M. A. Wolff, C. Schuck, N. Sinclair, M. Lončar, T. Komljenovic, D. Weld, S. Mookherjea, S. Buckley, M. Radulaski, S. Reitzenstein, B. Pingault, B. Machielse, D. Mukhopadhyay, A. Akimov, A. Zheltikov, G. S. Agarwal, K. Srinivasan, J. Lu, H. X. Tang, W. Jiang, T. P. McKenna, A. H. Safavi-Naeini, S. Steinhauer, A. W. Elshaari, V. Zwiller, P. S. Davids, N. Martinez, M. Gehl, J. Chiaverini, K. K. Mehta, J. Romero, N. B. Lingaraju, A. M. Weiner, D. Peace, R. Cernansky, M. Lobino, E. Diamanti, L. T. Vidarte, and R. M. Camacho, "2022 Roadmap on integrated quantum photonics," *Journal of Physics: Photonics*, vol. 4, p. 012501, Jan. 2022. Publisher: IOP Publishing.

[6] C. Sorace-Agaskar, C. Bruzewicz, P. Callahan, I. Chuang, E. Clements, P. Juodawlkis, D. Kharas, M. Kim, F. Knollmann, W. Loh, T. Mahony, R. Maxon, A. Medeiros, R. Morgan, D. Reens, M. Schuldt, R. Swint, G. West, R. McConnell, and J. Chiaverini, "Integrated Photonics for Trapped Ion-Based Quantum Computing and Sensing," in *2023 IEEE Photonics Society Summer Topicals Meeting Series (SUM)*, pp. 1–2, July 2023. ISSN: 2376-8614.

[7] R. McConnell, B. Aull, D. Braje, C. Bruzewicz, P. Callahan, J. Chiaverini, M. Collins, K. Donlon, B. Felton, P. Juodawlkis, D. Kharas, W. Loh, R. Niffenegger, D. Reens, K. Ryu, J. Sage, C. Sorace-Agaskar, J. Stuart, and G. West, "Integrated Technologies for Portable Optical Clocks," in *OSA Optical Sensors and Sensing Congress 2021 (AIS, FTS, HISE, SENSORS, ES) (2021), paper SW4I.1*, p. SW4I.1, Optica Publishing Group, July 2021.

[8] K. K. Mehta and R. J. Ram, "Precise and diffraction-limited waveguide-to-free-space focusing gratings," *Scientific Reports*, vol. 7, p. 2019, May 2017. Number: 1 Publisher: Nature Publishing Group.

[9] U. Saha, J. D. Siverns, J. Hannegan, M. Prabhu, Q. Quraishi, D. Englund, and E. Waks, "Routing Single Photons from a Trapped Ion Using a Photonic Integrated Circuit," *Physical Review Applied*, vol. 19, p. 034001, Mar. 2023. Publisher: American Physical Society.

[10] C. Sorace-Agaskar, D. Kharas, S. Yegnanarayanan, R. T. Maxson, G. N. West, W. Loh, S. Bramhavar, R. J. Ram, J. Chiaverini, J. Sage, and P. Juodawlkis, "Versatile Silicon Nitride and Alumina Integrated Photonic Platforms for the Ultraviolet to Short-Wave Infrared," *IEEE Journal of Selected Topics in Quantum Electronics*, vol. 25, pp. 1–15, Sept. 2019. Conference Name: IEEE Journal of Selected Topics in Quantum Electronics.

[11] M. K. Joshi, A. Fabre, C. Maier, T. Brydges, D. Kiesenhofer, H. Hainzer, R. Blatt, and C. F. Roos, "Polarization-gradient cooling of 1D and 2D ion Coulomb crystals," *New Journal of Physics*, vol. 22, p. 103013, Oct. 2020. Publisher: IOP Publishing.

[12] C. F. Roos, D. Leibfried, A. Mundt, F. Schmidt-Kaler, J. Eschner, and R. Blatt, "Experimental Demonstration of Ground State Laser Cooling with Electromagnetically Induced Transparency," *Physical Review Letters*, vol. 85, pp. 5547–5550, Dec. 2000. Publisher: American Physical Society.

[13] A. Hattori, S. Corsetti, T. Sneh, M. Notaros, R. Swint, P. T. Callahan, C. D. Bruzewicz, F. Knollmann, R. McConnell, J. Chiaverini, and J. Notaros, "Integrated-Photonics-Based Architectures for Polarization-Gradient and EIT Cooling of Trapped Ions," in *Frontiers in Optics + Laser Science 2022 (FIO, LS) (2022), paper FM4B.3*, p. FM4B.3, Optica Publishing Group, Oct. 2022.

[14] L. Soldano and E. Pennings, "Optical multi-mode interference devices based on self-imaging: principles and applications," *Journal of Lightwave Technology*, vol. 13, pp. 615–627, Apr. 1995. Conference Name: Journal of Lightwave Technology.

[15] J. Notaros, C. V. Poulton, M. Raval, and M. R. Watts, "Near-Field-Focusing Integrated Optical Phased Arrays," *Journal of Lightwave Technology*, vol. 36, pp. 5912–5920, Dec. 2018. Publisher: IEEE.

[16] T. Sneh, A. Hattori, M. Notaros, S. Corsetti, and J. Notaros, "Design of Integrated Visible-Light Polarization Rotators and Splitters," in *Frontiers in Optics + Laser Science 2022 (FIO, LS) (2022), paper JTu5A.48*, p. JTu5A.48, Optica Publishing Group, Oct. 2022.

[17] A. Hattori, T. Sneh, M. Notaros, S. Corsetti, P. T. Callahan, J. Chiaverini, and J. Notaros, "Integrated Visible-Light Polarization Rotators and Splitters for Atomic Quantum Systems," *Under Review*.

[18] C. Sun, Y. Yu, Y. Ding, Z. Li, W. Qi, and X. Zhang, "Integrated mode-transparent polarization beam splitter supporting thirteen data channels," *Photonics Research*, vol. 8, pp. 978–985, June 2020. Publisher: Optica Publishing Group.

[19] M. R. Watts and H. A. Haus, "Integrated mode-evolution-based polarization rotators," *Optics Letters*, vol. 30, pp. 138–140, Jan. 2005. Publisher: Optica Publishing Group.

[20] M. R. Watts, H. A. Haus, and E. P. Ippen, "Integrated mode-evolution-based polarization splitter," *Optics Letters*, vol. 30, pp. 967–969, May 2005. Publisher: Optica Publishing Group.

[21] F. Zhang, J. Zheng, Y. Song, W. Liu, P. Xu, and A. Majumdar, "Ultra-broadband and compact polarizing beam splitter in silicon photonics," *OSA Continuum*, vol. 3, pp. 560–567, Mar. 2020. Publisher: Optica Publishing Group.

[22] S. Lin, J. Hu, and K. B. Crozier, "Ultracompact, broadband slot waveguide polarization splitter," *Applied Physics Letters*, vol. 98, p. 151101, Apr. 2011.

[23] K. Gallacher, P. F. Griffin, E. Riis, M. Sorel, and D. J. Paul, "Silicon nitride waveguide polarization rotator and polarization beam splitter for chip-scale atomic systems," *APL Photonics*, vol. 7, p. 046101, Apr. 2022.

[24] J. M. Hong, H. H. Ryu, S. R. Park, J. W. Jeong, S. G. Lee, E.-H. Lee, S.-G. Park, D. Woo, S. Kim, and B.-H. O, "Design and fabrication of a significantly shortened multimode interference coupler for polarization splitter application," *IEEE Photonics Technology Letters*, vol. 15, pp. 72–74, Jan. 2003. Conference Name: IEEE Photonics Technology Letters.

[25] D. Dai, Z. Wang, J. Peters, and J. E. Bowers, "Compact Polarization Beam Splitter Using an Asymmetrical Mach–Zehnder Interferometer Based on Silicon-on-Insulator Waveguides," *IEEE Photonics Technology Letters*, vol. 24, pp. 673–675, Apr. 2012. Conference Name: IEEE Photonics Technology Letters.

[26] D. Dai and J. E. Bowers, "Novel concept for ultracompact polarization splitter-rotator based on silicon nanowires," *Optics Express*, vol. 19, pp. 10940–10949, May 2011. Publisher: Optica Publishing Group.

[27] Z. Wang and D. Dai, "Ultrasmall Si-nanowire-based polarization rotator," *JOSA B*, vol. 25, pp. 747–753, May 2008. Publisher: Optica Publishing Group.

[28] H. Fukuda, K. Yamada, T. Tsuchizawa, T. Watanabe, H. Shinojima, and S.-i. Itabashi, "Polarization rotator based on silicon wire waveguides," *Optics Express*, vol. 16, pp. 2628–2635, Feb. 2008. Publisher: Optica Publishing Group.

[29] L. Liu, Y. Ding, K. Yvind, and J. M. Hvam, "Silicon-on-insulator polarization splitting and rotating device for polarization diversity circuits," *Optics Express*, vol. 19, pp. 12646–12651, June 2011. Publisher: Optica Publishing Group.

[30] J. M. F. Cabanillas, M. K. Singh, B. Zhang, and M. A. Popović, "Compact Broadband Rapid-Adiabatic Polarization Splitter- Rotators in a Monolithic Electronic-Photonic SOI Platform," in *Conference on Lasers and Electro-Optics (2021), paper SW4E.2*, p. SW4E.2, Optica Publishing Group, May 2021.

[31] W. D. Sacher, Y. Huang, L. Ding, T. Barwicz, J. C. Mikkelsen, B. J. F. Taylor, G.-Q. Lo, and J. K. S. Poon, "Polarization rotator-splitters and controllers in a Si_3N_4-on-SOI integrated photonics platform," *Optics Express*, vol. 22, pp. 11167–11174, May 2014. Publisher: Optica Publishing Group.

[32] D. DeSantis, M. Notaros, M. R. Torres, and J. Notaros, "Underwater Wireless Optical Communications Using Integrated Optica Phased Arrays," in *Proceedings of IEEE Photonics Conference (IPC)*, 2023.

[33] F. Hufnagel, A. Sit, F. Grenapin, F. Bouchard, K. Heshami, D. England, Y. Zhang, B. J. Sussman, R. W. Boyd, G. Leuchs, and E. Karimi, "Characterization of an underwater channel for quantum communications in the Ottawa River," *Optics Express*, vol. 27, pp. 26346–26354, Sept. 2019. Publisher: Optica Publishing Group.

[34] S.-C. Zhao, X.-H. Han, Y. Xiao, Y. Shen, Y.-J. Gu, and W.-D. Li, "Performance of underwater quantum key distribution with polarization encoding," *JOSA A*, vol. 36, pp. 883–892, May 2019. Publisher: Optica Publishing Group.

[35] C. Ropp, W. Zhu, A. Yulaev, D. Westly, G. Simelgor, A. Rakholia, W. Lunden, D. Sheredy, M. M. Boyd, S. Papp, A. Agrawal, and V. Aksyuk, "Integrating planar photonics for multi-beam generation and atomic clock packaging on chip," *Light: Science & Applications*, vol. 12, p. 83, Apr. 2023. Number: 1 Publisher: Nature Publishing Group.

[36] A. Isichenko, N. Chauhan, D. Bose, J. Wang, P. D. Kunz, and D. J. Blumenthal, "Photonic integrated beam delivery for a rubidium 3D magneto-optical trap," *Nature Communications*, vol. 14, p. 3080, May 2023. Number: 1 Publisher: Nature Publishing Group.

[37] S. Corsetti, A. Hattori, R. Swint, M. Notaros, G. N. West, T. Sneh, F. Knollmann, P. T. Callahan, T. Mahony, E. R. Clements, C. Sorace-Agaskar, D. Kharas, R. McConnell, J. Chiaverini, and J. Notaros, "Integrated Polarization-Diverse Grating Emitters for Trapped-Ion Quantum Systems," *Under Review*.

[38] G. Spektor, D. Carlson, Z. Newman, J. L. Skarda, N. Sapra, L. Su, S. Jammi, A. R. Ferdinand, A. Agrawal, J. Vučković, and S. B. Papp, "Universal visible emitters in nanoscale integrated photonics," *Optica*, vol. 10, pp. 871–879, July 2023. Publisher: Optica Publishing Group.

[39] J. Notaros, F. Pavanello, M. T. Wade, C. M. Gentry, A. Atabaki, L. Alloatti, R. J. Ram, and M. A. Popović, "Ultra-Efficient CMOS Fiber-to-Chip Grating Couplers," in *Optical Fiber Communication Conference (2016), paper M2I.5*, p. M2I.5, Optica Publishing Group, Mar. 2016.